

# Electron-spin-resonance meanderlines for effective spin control in Si quantum dots for large-scale qubit applications

Yao-Chun Chang,<sup>1</sup> Ian Huang,<sup>2</sup> Chiung-Yu Chen,<sup>2</sup> Min-Jui Lin,<sup>3</sup> Shih-Yuan Chen,<sup>2,3, a)</sup> and Jiun-Yun Li<sup>1,3,4, a)</sup>

<sup>1)</sup>*Graduate Institute of Electronics Engineering, National Taiwan University, Taipei 10617, Taiwan*

<sup>2)</sup>*Graduate Institute of Communication Engineering, National Taiwan University, Taipei 10617, Taiwan*

<sup>3)</sup>*Department of Electrical Engineering, National Taiwan University, Taipei 10617, Taiwan*

<sup>4)</sup>*Taiwan Semiconductor Research Institute, Hsin-Chu 300091, Taiwan*

Coherent control of electron spins in multiple quantum dots (QD) is critical for realizing large-scale spin qubits. The manipulation of electron spins in Si QDs can be achieved by electron spin resonance (ESR). While the effective spin control over a single qubit has been demonstrated, the architecture of ESR lines for large-scale spin qubits has yet to be demonstrated. In this paper, we propose an ESR meanderline for large-scale Si QDs. Simulation results show that magnetic fields can be effectively enhanced with low electric fields using a meanderline, enabling high-fidelity and low-noise control over electron spins in a 50-qubit system. Reflection coefficients of ESR meanderlines by on-wafer microwave measurements show low loss (-7 dB) for a 3-qubit device at a frequency range of 10 to 50 GHz.

Quantum computers are predicted to solve some complex problems substantially faster than classical computers<sup>1,2</sup>. Spin-based Si quantum dots (QDs) have been considered a promising candidate for high-fidelity quantum bits (qubits) due to long-lived spin states by the enrichment of <sup>28</sup>Si isotopes<sup>3,4</sup>. Scalable spin-based qubits can be implemented on Si-<sup>5</sup> or Ge-based<sup>6,7</sup> heterostructures by the mature VLSI technology. To perform coherent control over carrier spins for large-scale qubits, the techniques of electric dipole spin resonance (EDSR)<sup>8</sup> or electron spin resonance (ESR)<sup>9</sup> have been used. For the EDSR technique, an oscillating magnetic field is created by applying ac voltages on the gate electrodes. EDSR can be done through the effects of spin-orbit coupling (SOC)<sup>10,11</sup> or a magnetic-field gradient using micromagnets<sup>12,13</sup>. However, the decoherence time ( $T_2$ ) becomes shorter due to the effects of SOC<sup>14</sup>, and the required complicated layout design of micromagnets might also hamper the EDSR control for large-scale QD arrays. For ESR control, an oscillating magnetic field is generated from alternating current through a transmission line to induce spin flips by matching the frequency of the magnetic field to the Larmor frequency of the spin states<sup>15,16</sup>. Using the technique of frequency-division multiple access (FDMA)<sup>17</sup>, spins in multiple qubits can be controlled individually by electrically tuning the resonance frequency of the ESR line via the Stark effect<sup>16,18</sup>.

While much prior work have focused on optimizing the ESR design for the detection of spin ensembles<sup>19,20</sup> or the control for single qubits<sup>21–23</sup>, the spin control over large-scale qubits has not been addressed. In this paper, we demonstrate an ESR device for high-fidelity spin control in large-scale Si QD arrays. In the proposed meanderline structure, large magnetic fields perpendicular to the device plane with small electric fields are generated at the locations of QDs, leading to higher spin flipping rates and reduced charge noise or heating

effects, respectively. Furthermore, the distributions of magnetic fields are uniform across  $\sim 6 \mu\text{m}$ , enabling coherent control in a 50-qubit system. We simulate the distributions of electromagnetic (EM) fields generated by the ESR meanderlines using HFSS<sup>24</sup>, a commercial 3D EM solver based on a finite element method (FEM). Then, we fabricated the devices by standard microfabrication steps and analyze their reflection coefficient ( $S_{11}$ ) since the meanderline is a one-port device (see Supplementary Materials). The simulation results show that a large magnetic field ( $|B_{AC}|$ ) of  $> 10 \text{ mT}$  is achieved with a small electric field ( $|E_{AC}|$ ) of  $< 0.01 \text{ MV/m}$  to suppress local heating and reduce charge noise for single-qubit control. For multiple qubits ( $\sim 50$  qubits),  $|B_{AC}|$  is still larger than  $9 \text{ mT}$  with a  $|E_{AC}|$  below  $0.2 \text{ MV/m}$ , which is better than a conventional ESR structure for single-qubit control<sup>15,25</sup>. The amplitude of reflection coefficients ( $|S_{11}|$ ) of the fabricated meanderline device is larger than -7 dB for a 3-qubit system at a frequency range from 10 to 50 GHz. The proposed meanderline devices enable high-fidelity operations of large-scale spin-based Si qubits by high magnetic fields and low electric fields.

The device structure of the meanderline is illustrated in Fig. 1(a), with a QD surrounded by its three arms. The oscillating magnetic field is maximized at the location of the QD to increase the Rabi frequency ( $f_{Rabi} = g\mu_B|B_{AC}|/2h$ , where  $g$  is g-factor,  $\mu_B$  is Bohr magneton, and  $h$  is Planck constant) for high-fidelity qubit operations<sup>17</sup>. The magnetic fields generated by the electric current flowing in those three arms are expected to be stronger than that by a conventional ESR line<sup>25</sup>. On the other hand, the associated oscillating electric field should be minimized to avoid photon-assisted tunneling<sup>15</sup> and local heating<sup>25</sup> to improve the fidelity. The meanderline structure can also minimize electric fields due to the proximity of its multiple arms to the QDs with the boundary conditions of zero electric fields at the surface of the ESR lines<sup>26</sup>. In this work, we adopt a linear QD array<sup>22</sup> integrated with the proposed ESR meanderline to simulate EM-field distributions [Figs. 1(b) and 1(c)]. The ESR meanderlines and QD gates are isolated from the Si substrate by a layer of  $\text{Al}_2\text{O}_3$ , while the isolation between them was done by  $\text{SiO}_2$ . The QD gates

<sup>a)</sup> Authors to whom correspondence should be addressed:  
shihyuan@ntu.edu.tw and jiunyun@ntu.edu.tw

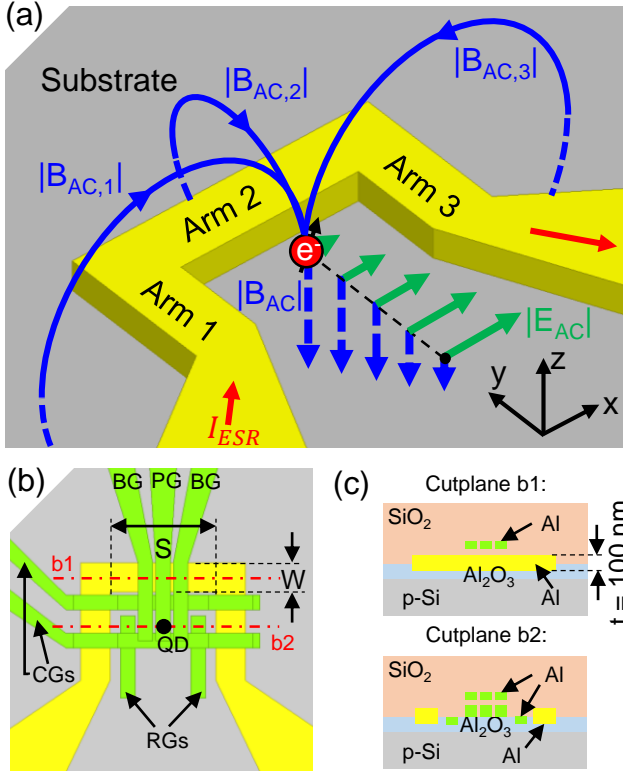


FIG. 1. (a) Device structure of an ESR meanderline. The yellow region represents the aluminum meanderline carrying alternating current. (b) Top and (c) side views of the ESR meanderline surrounding a QD. All green electrodes are aluminum QD gates. PG: plunger gate; BG: barrier gate; CG: confinement gate; RG: reservoir gate. All QD gates are biased to 0 V (grounded).  $W$  is the meanderline width,  $S$  is the gap width, and  $t$  is the metal thickness of ESR meanderlines.

effectively suppress  $|E_{AC}|$  at the location of the QD due to the screening effects. The simulation results show that  $|S_{11}|$  for the devices with and without QD gates only differs by less than 0.5 dB. Thus, QD gates are only considered for the simulation of EM-field distributions but not for the characterization of reflection coefficients of the fabricated meanderline devices in this work.

First, we simulate the EM fields generated by the ESR meanderline. The material parameters used for the simulation are listed in Table I. The simulated contours of the amplitude of the oscillating EM fields at the Si surface and along a cut-plane crossing the QD are illustrated in Fig. 2(a). Since the QD is surrounded by three arms of the meanderline, the magnetic fields are enhanced effectively. Along the cut-plane A [Fig. 2(b)], the magnetic field is strongest ( $\sim 30$  mT) near the two arms (arm 1 and 3) of the meanderline. At the center of the gap (midpoint between those two arms), the magnetic field is  $\sim 20$  mT, which is two times larger than the previously reported in Ref. 25, given the same input power of 0 dBm and excitation frequency of 30 GHz. On the other hand, low electric fields are achieved at the location of the QD due to its proximity to arm 2 with the imposed boundary condition of zero tangential electric fields at the conductor surface

TABLE I. Material properties of EM fields simulation.

Materials	Permittivity	Permeability	Conductivity (S/m)
Al	$\epsilon_0$	$\mu_0$	$3.8 \times 10^7$
Si	$11.7\epsilon_0$	$\mu_0$	$10$ ( $\rho = 10 \Omega\text{-cm}$ )
SiO <sub>2</sub>	$4\epsilon_0$	$\mu_0$	0
Al <sub>2</sub> O <sub>3</sub>	$9.8\epsilon_0$	$\mu_0$	0

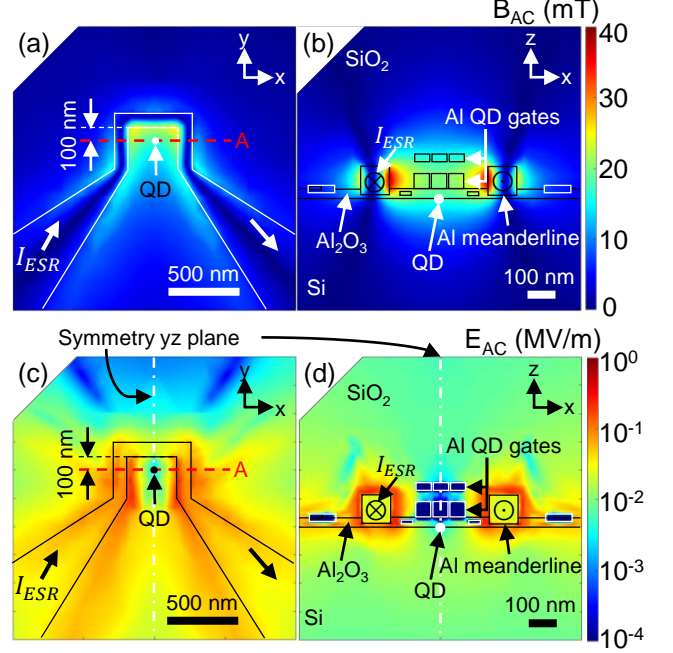


FIG. 2. (a) Top and (b) side views of the simulated contours of the amplitudes of the oscillating magnetic fields ( $|B_{AC}|$ ). (c) Top and (d) side views of the simulated contours of the amplitude of the oscillating electric fields ( $|E_{AC}|$ ). Input power at the input port of meanderlines is 0 dBm. QD gates are not plotted in (a) and (c) to provide a better view.

[Fig. 2(c)]. The screening effects by the QD gates further suppress the electric fields [Fig. 2(d)], which couple to the Al QD gates with high conductivity, but not directly through the QDs. Thus, the electric fields close to the QDs are significantly reduced ( $< 0.006$  MV/m) [Fig. 2(d)]. Note that the electric fields on a symmetry plane [marked in Figs. 2(c) and 2(d)] are small because the electric current flows in reverse directions on each side of the plane, making the symmetry plane a virtual ground plane<sup>26</sup>. Since there is no tangential component of the electric fields on a ground plane, the electric fields on the symmetry plane, where the QD is located, are extremely small.

The effects of the meanderline width ( $W$ ) and the gap ( $S$ ) between arms 1 and 3 on the distributions of EM fields are illustrated in Fig. 3. The EM fields are affected by the width of a meanderline owing to different distributions of the electric current across the ESR line. For a smaller  $W$ , current and charges are distributed closer to the center of the meanderline, leading to larger magnetic and electric fields<sup>26</sup> [Fig. 3(a)]. On the other hand, as the gap increases, both  $|B_{AC}|$  and  $|E_{AC}|$  are smaller due to the longer distance between arms 1 and 3 of the ESR line and the QD. The ratio of  $|B_{AC}|/|E_{AC}|$  increases with

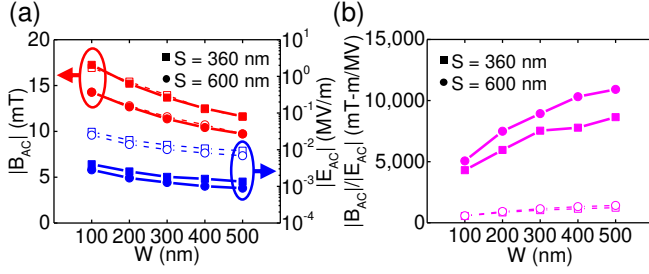


FIG. 3. (a) Simulated  $|B_{AC}|$ ,  $|E_{AC}|$ , and (b)  $|B_{AC}|/|E_{AC}|$  ratio at the QD location by ESR meanderlines vs. line width ( $W$ ) for different gap widths ( $S$ ). The open symbols represent simulated results without any QD gate.

$W$  and  $S$ , showing that the electric field has a stronger dependence on the width of the ESR line than the magnetic field. Since the QD gates could screen the electric fields generated by the ESR line, we also simulated the field distributions without any QD gates underneath (open symbols). While  $|B_{AC}|$  is not affected by the QD gates,  $|E_{AC}|$  is enhanced by a factor of ten, leading to a smaller  $|B_{AC}|/|E_{AC}|$  ratio. However, even without any QD gate, the proposed ESR meanderline still outperforms the conventional ESR line presented in Ref. 25 by an order of magnitude in terms of the  $|B_{AC}|/|E_{AC}|$  ratio.

We now enlarge the ESR meanderline structure to include more QDs by increasing the gap. The distributions of EM fields for a 3-qubit device are illustrated in Figs. 4(a) and 4(b). The results are similar to those for a single QD (Fig. 2), while the amplitudes are smaller due to smaller contributions of arms 1 and 3 caused by the larger gap. The variation of the magnetic fields along the cutlines across the QD array is small ( $\sim 6.5\%$ ) between the QDs at the center and on both sides [Fig. 4(c)]. The electric fields on the QDs at both sides are larger than that on the central QD due to the shorter distance between the QDs at both sides and the side arms of the meanderline.

For multi-qubit operations, spins in different qubits can be manipulated by RF signals with different frequencies through the ESR meanderline by the FDMA technique<sup>17</sup>. By specific designs of the microwave pulse shapes, spin qubits with different Larmor frequencies can be controlled simultaneously<sup>17,27</sup>. We simulated the frequency responses of  $|B_{AC}|$  and  $|E_{AC}|$  generated by the meanderline with different gaps [Fig. 5(a)]. Both  $|B_{AC}|$  and  $|E_{AC}|$  change with the frequency slightly since the scale of the meanderline ( $< 10 \mu\text{m}$ ) is much smaller than the corresponding wavelengths of the RF signals for spin manipulation [ $\lambda = c/(\sqrt{\epsilon_r}f) > 1 \text{ mm}$  for  $10 \text{ GHz} < f < 50 \text{ GHz}$ ]. Thus, the ESR meanderline is operated in the quasi-static regime and insensitive to the variations in frequency. A wider operational frequency range is desirable because more RF channels are allowed in the ESR line to control more spin qubits via FDMA<sup>17</sup>. In addition, the Larmor frequency should be sufficiently larger than the Rabi frequency for the rotating-wave approximation to hold for a high gate fidelity<sup>17</sup>. Otherwise, the eigenstates of the spin are disturbed by ac magnetic fields during the spin flipping process, reducing the spin relaxation time ( $T_1$ ).

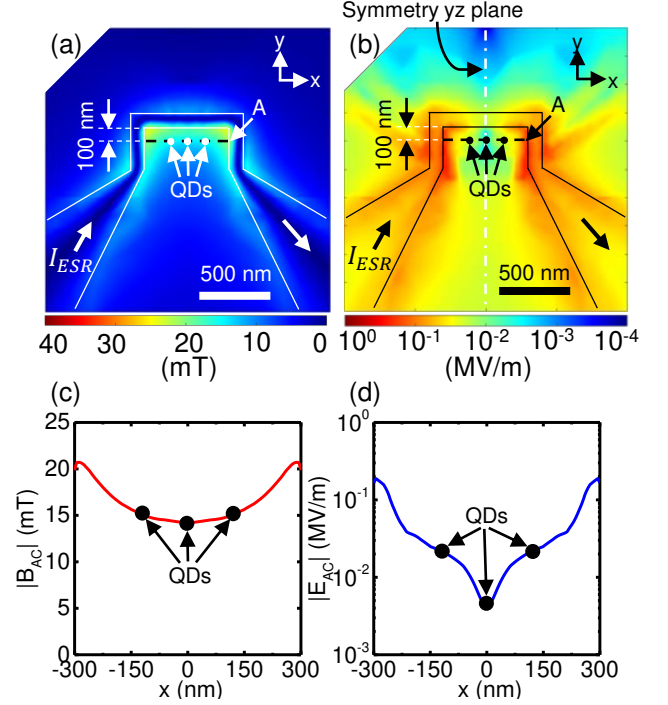


FIG. 4. Simulated contours of the amplitudes of the oscillating (a) magnetic fields ( $|B_{AC}|$ ) and (b) electric fields ( $|E_{AC}|$ ) for an ESR meanderline ( $S = 600 \text{ nm}$ ) surrounding a linear array of three QDs. (c)  $|B_{AC}|$  and (d)  $|E_{AC}|$  along the cutline A in (a) and (b). QD gates are not plotted in (a) and (b) to provide a better view.

To investigate the effects of the gap in the meanderline, we simulated EM fields at the center of the gap and the QD next to the side arms (arm 1 or 3) of the ESR meanderlines [Figs. 5(b) and 5(c)]. The average distance between each QD is 120 nm for the simulation, and the corresponding number of the qubits are indicated on the top axes of Figs. 5(b) to 5(d). EM fields at the center of the gap are smallest across the QD array, while the QDs next to the side arms experience the strongest EM fields. As the gap increases, the magnetic fields for all QDs decrease slightly due to the reduced contributions from the side arms. The magnetic field saturates to  $\sim 9 \text{ mT}$  as the qubit is scaled up since the contributions from both side arms become negligible and arm 2 dominates.

Similarly, the electric field at the center of the gap is slightly reduced and saturated due to the weaker contributions from the side arms. However,  $|E_{AC}|$  at the QDs next to the side arms increases with the gap. As the gap increases, arm 2 becomes longer, leading to a larger resistance and thus a larger voltage difference between the side arms. Thus, the electric fields between the side arms and the grounded QD gates are enhanced. The  $|B_{AC}|/|E_{AC}|$  ratio for the central QD is constant as the number of qubits increases and decreases for the QD next to the side arms of the meanderline. The minimum of the  $|B_{AC}|/|E_{AC}|$  ratio is still three times larger than previously reported using a single ESR line<sup>25</sup>.

Note that as the qubit number increases to 50, a meanderline will approximate to a conventional ESR line as in Ref. 25 since the contributions from two side arms becomes less than

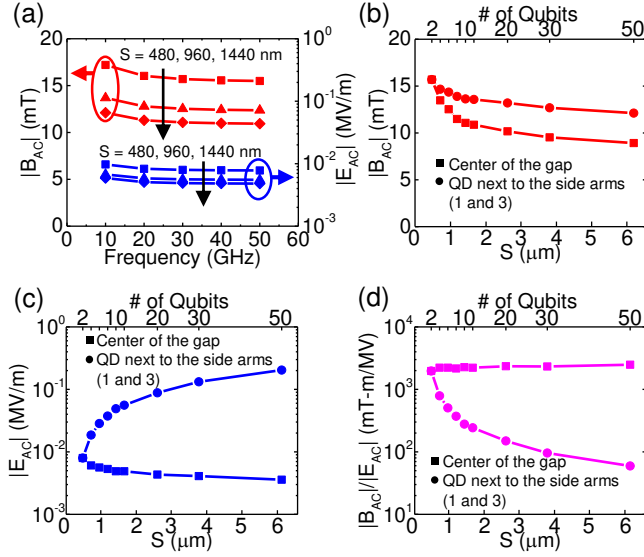


FIG. 5. Simulated frequency response of (a)  $|B_{AC}|$  and  $|E_{AC}|$  at the gap center of the meanderline with different gaps. (b) Simulated  $|B_{AC}|$ , (c)  $|E_{AC}|$ , and (d)  $|B_{AC}|/|E_{AC}|$  vs.  $S$  or number of qubits for the QDs at the center and next to the side arms of the meanderline.

that from the long arm (arm 2). To further scale up the qubit system, a multi-period meanderline can be used to accommodate more QDs<sup>28</sup>. With multiple periods, we can effectively scale up the qubit system while maintaining high magnetic fields and  $|B_{AC}|/|E_{AC}|$  ratios.

Next, we performed a network analysis on the ESR meanderlines through on-wafer microwave measurements and calibration techniques at room temperature (see Supplementary Materials). The microwave measurements were conducted using an Agilent E8361C PNA network analyzer. Coaxial cables and RF probes in a configuration of ground-signal-ground (GSG) with a  $100\text{-}\mu\text{m}$  probe pitch were used to transmit RF signals from the network analyzer to the ESR meanderlines via a balanced-to-unbalanced (balun) converter. In order to extract the reflection coefficients of the ESR meanderlines, a calibration technique of Thru-Reflect-Line (TRL)<sup>29</sup> was performed to eliminate the attenuation and phase delay contributed by the transmission lines, RF probes, and baluns between the network analyzer and the meanderline. The simulated  $|S_{11}|$  for all devices is independent of frequency (Fig. 6), which is attributed to the quasi-static nature of the meanderline. Note that the conductivity of Al for the simulation of reflection coefficients is  $1.5 \times 10^7$  S/m, acquired through the fitting of the simulated results to the experimental results at 50 GHz.  $|S_{11}|$  decreases as the line width decreases [Fig. 6(a)] because by assuming the electric current distributes uniformly across the ESR line, reducing the line width increases the resistance, leading to increased resistive loss and a reduced  $|S_{11}|$ . On the other hand, as the gap increases to include more QDs,  $|S_{11}|$  decreases owing to the increase of both resistive and radiative losses [Fig. 6(b)]. Since the short-circuited line near QDs [e.g., arm 2 in Fig. 2(a)] acts as a Hertzian dipole antenna<sup>30</sup>, there is more radiative loss for a longer ESR meanderline to accommodate more qubits.  $|S_{11}|$  of the meanderline

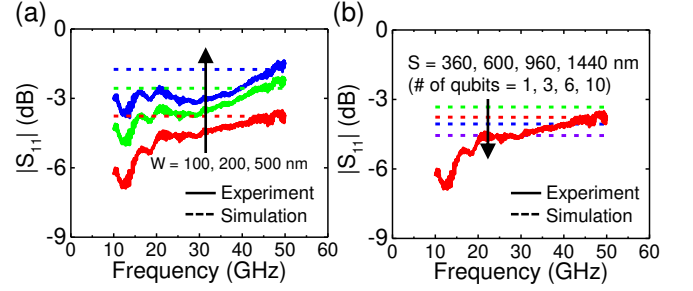


FIG. 6. Frequency responses of  $|S_{11}|$  of ESR meanderlines for different (a) line widths ( $W$ ) with  $S = 600$  nm and (b) gaps ( $S$ ) with  $W = 100$  nm.

for different widths and gaps are greater than  $-7$  dB at a frequency range of 10 to 50 GHz, which is comparable to the conventional ESR structure for single-qubit control<sup>25</sup>.

The measured reflection coefficients are consistent with the simulated results near 50 GHz (Fig. 6). However, as the frequency decreases, the measured  $|S_{11}|$  becomes smaller, while the simulations suggest it should be independent of frequency. It could be possibly due to the increased dielectric loss (mainly from Si) at lower frequencies<sup>31</sup>. The total dielectric loss tangent of a dielectric material is  $\tan\delta = \tan\delta_d + \sigma/\omega\epsilon_0\epsilon_r$ , where  $\tan\delta_d$  is the dielectric loss tangent due to pure dielectric loss mechanisms such as electronic and ionic polarization<sup>31</sup>,  $\sigma$  is the conductivity of the material,  $\omega$  is the angular frequency,  $\epsilon_0$  is the permittivity of vacuum, and  $\epsilon_r$  is the relative permittivity of the material. With larger  $\tan\delta$ , EM waves are attenuated more when propagating inside the dielectric material. Thus, at lower frequencies, the larger loss leads to a reduced  $|S_{11}|$ . The frequency-dependent dielectric loss was not considered for our simulation since we expect the dielectric loss to be negligible at a lower frequency at cryogenic temperatures due to the carrier freeze-out<sup>32</sup>. Further study on the characterization of  $|S_{11}|$  at cryogenic temperatures is required to investigate the effects on the spin control.

In conclusion, we propose an ESR meanderline with high magnetic fields and low electric fields for high-fidelity control over Si-based spin qubits. We perform the simulation to characterize distributions of EM fields generated by the ESR meanderline. By increasing the width and gap of the meanderline, the electric fields at the QD can be significantly reduced while the magnetic fields only decrease slightly, leading to an extremely high  $|B_{AC}|/|E_{AC}|$  ratio. Furthermore, by increasing the gap of the meanderline, more QDs are included; simulation results suggest that this meanderline can support effective spin control with high magnetic fields, low electric fields, and high  $|B_{AC}|/|E_{AC}|$  ratio for a 50-qubit system via the FDMA technique. The experimental results of reflection coefficients show great matches to the simulations with a difference of 3 dB at frequencies of 10 GHz to 50 GHz and suggest that the ESR meanderline effectively achieves spin manipulation for large-scale qubits.

See the supplementary material for details on the microwave measurement of ESR meanderlines.

The work at National Taiwan University (NTU) has been

supported by the Ministry of Science and Technology (110-2622-8-002-014- and 109-2627-M-002-003-) and the Ministry of Education through the Higher Education Sprout Projects (NTU core consortium: 110L892602).

## DATA AVAILABILITY

The data that support the findings of this study are available on request from the corresponding author. The data are not publicly available due to the restriction of intellectual properties.

## REFERENCES

- <sup>1</sup>C. H. Bennett and P. W. Shor, IEEE Trans. Inf. Theory **44**, 2724 (1998).
- <sup>2</sup>Lov K. Grover, Phys. Rev. Lett. **79**, 325 (1997).
- <sup>3</sup>D. Loss and D. P. DiVincenzo, Phys. Rev. A **57**, 120 (1998).
- <sup>4</sup>D. P. DiVincenzo, Science **270**, 255 (1995).
- <sup>5</sup>D. M. Zajac, T. M. Hazard, X. Mi, E. Nielsen, and J. R. Petta, Phys. Rev. Applied **6**, 054013 (2016).
- <sup>6</sup>N. W. Hendrickx, D. P. Franke, A. Sammak, G. Scappucci, and M. Veldhorst, Nature **577**, 487 (2020).
- <sup>7</sup>N. W. Hendrickx, W. I. L. Lawrie, M. Russ, F. van Riggelen, S. L. de Snoo, R. N. Schouten, A. Sammak, G. Scappucci, and M. Veldhorst, Nature **591**, 580 (2021).
- <sup>8</sup>V. N. Golovach, M. Borhani, and D. Loss, Phys. Rev. B **74**, 165319 (2006).
- <sup>9</sup>C. P. Poole, *Electron Spin Resonance: A Comprehensive Treatise on Experimental Techniques* (Dover Publications, New York, 1996).
- <sup>10</sup>R. M. Jock, N. T. Jacobson, P. Harvery-Collard, A. M. Mounce, V. Srinivasa, D. R. Ward, J. Anderson, R. Manginell, J. R. Wendt, M. Rudolph, T. Pluym, J. K. Gamble, A. D. Baczewski, W. M. Witzel, and M. S. Carroll, Nat. Commun. **9**, 1768 (2018).
- <sup>11</sup>R. Ferdous, K. W. Chan, M. Veldhorst, J. C. C. Hwang, C. H. Yang, H. Sahasrabudhe, G. Klimeck, A. Morello, A. S. Dzurak, and R. Rahman, Phys. Rev. B **97**, 241401(R) (2018).
- <sup>12</sup>M. Pioro-Ladrière, T. Obata, Y. Tokura, Y.-S. Shin, T. Kubo, K. Yoshida, T. Taniyama, and S. Tarucha, Nature Phys. **4**, 776 (2008).
- <sup>13</sup>J. Yoneda, K. Takeda, T. Otsuka, T. Nakajima, M. R. Delbecq, G. Allison, T. Honda, T. Kōdera, S. Oda, Y. Hoshi, N. Usami, K. M. Itoh, and S. Tarucha, Nature Nanotech. **13**, 102 (2018).
- <sup>14</sup>L. Chirrolli and G. Burkard, Adv. Phys. **57**, 225 (2008).
- <sup>15</sup>F. H. L. Koppens, C. Buizert, K. J. Tielrooij, I. T. Vink, K. C. Nowack, T. Meunier, L. P. Kouwenhoven, and L. M. K. Vandersypen, Nature **442**, 766 (2006).
- <sup>16</sup>M. Veldhorst, J. C. C. Hwang, C. H. Yang, A. W. Leenstra, B. de Ronde, J. P. Dehollain, J. T. Muhonen, F. E. Hudson, K. M. Itoh, A. Morello, and A. S. Dzurak, Nat. Nanotechnol. **9**, 981 (2014).
- <sup>17</sup>J. P. G. van Dijk, E. Kawakami, R. N. Schouten, M. Veldhorst, L. M. K. Vandersypen, M. Babaie, E. Charbon, and F. Sebastiano, Phys. Rev. Applied **12**, 044054 (2019).
- <sup>18</sup>M. Veldhorst, C. H. Yang, J. C. C. Hwang, W. Huang, J. P. Dehollain, J. T. Muhonen, S. Simmons, A. Laucht, F. E. Hudson, K. M. Itoh, A. Morello, and A. S. Dzurak, Nature **526**, 410 (2015).
- <sup>19</sup>R. Narkowicz, D. Suter, and R. Stonies, J. Magn. Reson. **175**, 275 (2005).
- <sup>20</sup>B. Simović, P. Studerus, S. Gustavsson, R. Leturcq, K. Ensslin, R. Schuhmann, J. Forrer, and A. Schweiger, Rev. Sci. Instrum. **77**, 064702 (2006).
- <sup>21</sup>M. Veldhorst, H. G. J. Eenink, C. H. Yang, and A. S. Dzurak, Nat. Commun. **8**, 1776 (2017).
- <sup>22</sup>C. Jones, M. A. Fogarty, A. Morello, M. F. Gyure, A. S. Dzurak, and T. D. Ladd, Phys. Rev. X **8**, 021058 (2018).
- <sup>23</sup>R. Li, L. Petit, D. P. Franke, J. P. Dehollain, J. Helsen, M. Steudtner, N. K. Thomas, Z. R. Yoscovits, K. J. Singh, S. Wehner, L. M. K. Vandersypen, J. S. Clarke, and M. Veldhorst, Sci. Adv. **4**, eaar3960 (2018).
- <sup>24</sup><https://www.ansys.com/products/electronics/ansys-hfss>
- <sup>25</sup>J. P. Dehollain, J. J. Pla, E. Siew, K. Y. Tan, A. S. Dzurak, and A. Morello, Nanotechnology **24**, 015202 (2013).
- <sup>26</sup>D. M. Pozar, *Microwave Engineering* (Wiley, New York, 2011).
- <sup>27</sup>W. Huang, M. Veldhorst, N. M. Zimmerman, A. S. Dzurak, and D. Culcer, Phys. Rev. B **95**, 075403 (2017).
- <sup>28</sup>G. Marrocco, IEEE Antennas Wirel. Propag. Lett. **2**, 302 (2003).
- <sup>29</sup>G. F. Engen and C. A. Hoer, IEEE Trans. Microw. Theory Techn. **27**, 987 (1979).
- <sup>30</sup>J. D. Kraus and R. J. Marhefka, *Antennas for All Applications* (McGraw-Hill, New York, 2002).
- <sup>31</sup>J. Krupka, P. Kamiński, R. Kozłowski, B. Surma, A. Dierlamm, and M. Kwestarz, Appl. Phys. Lett. **107**, 082105 (2015).
- <sup>32</sup>D. A. Neamen, *Semiconductor Physics and Devices: Basic Principles* (McGraw-Hill, New York, 2012).